The Electrochemical Society
Advancing solid state & electrochemical science & technology

Alternative Ni-Impregnated Mixed Ionic-Electronic Conducting Anode for SOFC Operation at High Fuel Utilization

To cite this article: S. Futamura *et al* 2017 *J. Electrochem. Soc.* **164** F3055

View the article online for updates and enhancements.

Alternative Ni-Impregnated Mixed Ionic-Electronic Conducting Anode for SOFC Operation at High Fuel Utilization

S. Futamura,[a] Y. Tachikawa,[a,b,c,]* J. Matsuda,[b,d] S. M. Lyth,[d] Y. Shiratori,[a,b,c,d] S. Taniguchi,[b,d,e] and K. Sasaki[a,b,c,d,e,]*,z

[a]*Department of Hydrogen Energy Systems, Kyushu University, Nishi-ku, Fukuoka 819-0395, Japan*
[b]*Center for Co-Evolutional Social Systems, Kyushu University, Nishi-ku, Fukuoka 819-0395, Japan*
[c]*Next-Generation Fuel Cell Research Center (NEXT-FC), Kyushu University, Nishi-ku, Fukuoka 819-0395, Japan*
[d]*International Institute for Carbon-Neutral Energy Research (WPI-I2CNER), Kyushu University, Nishi-ku, Fukuoka 819-0395, Japan*
[e]*International Research Center for Hydrogen Energy, Kyushu University, Nishi-ku, Fukuoka 819-0395, Japan*

Redox-stable anodes are developed for zirconia-based electrolyte-supported SOFCs in order to improve the durability against fuel supply interruption and for higher fuel utilization, as an alternative to the conventional Ni-YSZ cermet. GDC ($Ce_{0.9}Gd_{0.1}O_2$) is utilized as a mixed ionic-electronic conductor (MIEC), and combined with LST ($Sr_{0.9}La_{0.1}TiO_3$) as an electronic conductor. Ni catalyst nanoparticles are incorporated via impregnation. The electrochemical characteristics of SOFC single cells using these anode materials are investigated in humidified H_2 at 800°C. The stability against redox cycling and under high fuel utilization is analyzed and discussed. Ni-impregnated anodes with dispersed Ni catalyst nanoparticles on conducting oxide LST-GDC backbones exhibit lower anode non-ohmic overvoltage, and improve I-V performance. These anodes also show better redox stability compared to conventional anodes because of the isolation of Ni catalysts, preventing their agglomeration. Moreover, the co-impregnation of Ni catalysts and GDC nanoparticles further improves electrochemical characteristics due to a decrease in anode ohmic (IR) loss and non-ohmic overvoltage. This anode shows comparable I-V performance to conventional anodes for typical humidified hydrogen fuels, and is a promising redox-stable alternative for application at high fuel utilization.

Solid oxide fuel cells (SOFCs) are promising electrochemical energy conversion systems that can directly produce electricity from chemical fuels, without combustion. The operating temperature is generally around 800°C, leading to several advantages including high electric conversion efficiency, fuel flexibility, and noble-metal-free fabrication. For example, in Japan, the commercialization of SOFCs as residential co-generation systems started in 2011. The electric efficiency reached a lower heating value (LHV) of 52% in 2016. Development of these systems for industrial applications is also in progress, and combining them with micro gas turbines and/or steam turbines can achieve even higher electric efficiency.[1]

The porous Ni yttrium-stabilized-zirconia (YSZ) cermet has been used as a conventional SOFC anode material for decades. However, the electron conducting pathways through the Ni metal phase (which also acts as the electrocatalyst) can be easily destroyed by redox reactions during potential cycling, where Ni redox reactions result in significant changes in volume. This leads to crack formation in the ionic conducting YSZ phase, and deterioration of the electrochemical performance, especially during e.g. system shutdown, fuel supply interruption, and at high fuel utilization.[2–8] Therefore, extra hydrogen (or hydrogen-containing gas) is often required during system shutdown in order to maintain reducing conditions on the anode side of the device at all times. The fuel utilization in practical systems must also be kept low for the same reason. Higher efficiency is required for wide-spread commercialization of SOFCs in the future, and therefore tolerance of higher fuel utilizations is desired.

Strontium titanate ($SrTiO_3$) with a perovskite structure has excellent chemical and physical stability in both oxidizing and reducing atmospheres under SOFC operating conditions. The electrical conductivity of this material is not sufficiently high,[9–15] but it can be enhanced by controlling the cation doping. One candidate anode material, that has been considered over years is lanthanum-doped strontium titanate (LST, $Sr_{0.9}La_{0.1}TiO_3$). LST has received much attention as an alternative SOFC anode material. Wang et al.[9,10] and Marina et al.[11] reported the thermal and electrocatalytic properties of $(La_xSr_{1-x})TiO_3$ under SOFC operating conditions. The thermal expansion coefficient of air-sintered $Sr_{0.9}La_{0.1}TiO_3$ is 11×10^{-6}/°C, which is close to that of electrolyte materials, and the electronic conductivity is sufficiently high under SOFC anode conditions.[16] In addition, the P_{O_2}-dependent expansion of air-sintered $(La_xSr_{1-x})TiO_3$ is negligible over a wide P_{O_2} range. Sun et al. have reported the performance of $(La_{0.4}Sr_{0.6})TiO_3$-based anodes,[12] and Yoo et al. have evaluated $(La_{0.2}Sr_{0.8})TiO_3$-based anode materials.[13,14]

The impregnation method is a popular approach for the preparation of well-dispersed catalysts through low-temperature decomposition, and has been used to improve redox stability due to structural advantages.[17–19] Several researchers have analyzed the properties of such catalyst-impregnated SOFC anodes over the years.[20] For example, Park et al. investigated the performance of Cu, Sn, and Rh impregnated anodes for internal reforming of butane fuel.[20] By dispersing MIEC catalysts, such as $Gd_xCe_{1-x}O_2$, on anode backbones increases in reaction site densities and/or suppression of carbon deposition have been observed.[21–24] Chen et al.[21] and Wang et al.[22] reported that the impregnation of $Gd_{0.2}Ce_{0.8}O_2$ into Ni-based anodes could suppress carbon deposition in the presence of weakly humidified hydrocarbon fuels. Shen et al. indicated that well-dispersed catalyst nanoparticles on $(La_{0.1}Sr_{0.9})TiO_3$ backbones formed via impregnation achieved much better redox stability.[23,24] In addition, Hussain et al. and Yurkiv et al. investigated Ni-ceria-impregnated $SrTiO_3$-based anodes for low temperature SOFCs.[25–27] Whilst much attention has been given to alternative anode materials for higher performance or better redox stability, few studies have concentrated on SOFC durability at high fuel utilization, which generally causes anode degradation, associated with Ni redox cycling. Fuel utilization is extremely important

for future wide-spread commercialization of SOFC systems, and thus alternative redox stable anodes should be developed for high fuel utilization, with comparable performance to conventional anodes.

In this study, we combine GDC ($Ce_{0.9}Gd_{0.1}O_2$) as a MIEC, with LST as an electronic conductor, resulting in a redox-stable SOFC anode backbone. This is used as an alternative to conventional Ni-zirconia cermet anodes in zirconia-based electrolyte-supported SOFC cells. The electrochemical characteristics and stability of SOFC single cells using these new anodes are investigated in humidified H_2 at 800°C. The concept of this study is to prepare a stable backbone using three different oxides and/or metal materials, each of which acts as a MIEC, an electronic conductor, or as an electrocatalyst. Ni catalyst nanoparticles are then homogeneously decorated onto the conducting backbones via co-impregnation with the MIEC, GDC. The aim of this study is to develop alternative SOFC anodes for high fuel utilization, with electrochemical characteristics and durability comparable to those of conventional anodes.

Experimental

Cell fabrication.—Figure 1a shows a schematic diagram of the SOFC single button cell used in this study. Scandia-stabilized zirconia (ScSZ) plates (10 mol% Sc_2O_3 - 1 mol% CeO_2 - 89 mol% ZrO_2, Dai-ichi Kigenso Kagaku Kogyo Co., Ltd., Osaka, Japan) with a diameter of 20 mm and a thickness of 200 μm were used as solid electrolytes. Anode powders were prepared by mixing LST ($La_{0.1}Sr_{0.9}TiO_3$, Prax-air, Inc., CT, USA) and GDC ($Gd_{0.1}Ce_{0.9}O_2$, Rhodia, ULSA grade, USA) in a 50:50 ratio by volume. Anode paste was prepared by blending the anode powders with organic binder (α-terpineol). Cathode paste for the functional layer was made with lanthanum strontium manganite (LSM, $(La_{0.8}Sr_{0.2})_{0.98}MnO_3$, Praxair, USA) and ScSZ powders in a 47:53 ratio by volume. The current-collecting cathode layer comprised LSM powder.[4]

Porous anode layers were screen-printed onto the ScSZ electrolyte plates, followed by sintering in air at 1300°C for 3 h. Cathode layers were screen-printed onto the counter side of the ScSZ electrolyte plates, followed by sintering in air at 1200°C for 5 h. Figure 1a shows the thickness of each layer after sintering. In addition, a thin buffer layer of GDC with a thickness of around 5 μm, was used at the interface between the anode and the electrolyte, followed by sintering in air at 1400°C for 2 h.

For the impregnation step, the prepared porous anode layer was then soaked with an aqueous Ni-impregnation solution of $Ni(NO_3)_2·6H_2O$ (Kishida Chemicals Co., Ltd., Japan), or an aqueous Ni-GDC co-impregnation solution of $Ni(NO_3)_2·6H_2O$, $Gd(NO_3)_3·6H_2O$ (Kanto Chemical Co., Inc., Japan), and $Ce(NO_3)_3·6H_2O$ (Kishida Chemicals Co., Ltd., Japan). The co-impregnation step was performed using different GDC mixing volume ratios. The impregnation steps were followed by thermal decomposition in air at 1000°C for 2 h, to obtain nanoparticles of NiO and/or GDC decorated on the electrode backbone. Phase identification of the synthesized SOFC anode materials was performed by X-ray diffraction (XRD, Cu Kα radiation, Rigaku RINT Ultima III, Japan).

A reference electrode (RE) with a geometric area of ca. 0.04 cm^2 was then painted ca. 2 mm away from the edge of the cathode, using Pt paste. Since the anode potential was measured between the anode and the reference electrode on the cathode side, it has a higher value than the cell voltage by the potential difference between the cathode and the reference electrode. Pt mesh (80 mesh acting) was attached to each electrode surface as a current collector. The thickness and the geometric area of the electrode layers were approximately 40 μm and 8 × 8 mm^2 (0.64 cm^2), respectively.

Cell test.—Figure 1b shows the electrochemical experimental setup. Before measuring the electrochemical characteristics, the cell was heated up to 1000°C at a rate of 200°C h^{-1}, in order to melt the Pyrex glass powder and seal the cell. 3%-humidified H_2 gas was subsequently supplied to the anode for 1 h at 100 mL min^{-1}, in order to reduce NiO to Ni metal. Cell performance (I-V characteristics, anode

IR losses, and anode non-ohmic overvoltage) was measured at 800°C utilizing differently humidified hydrogen gas. The anode voltage was measured as the voltage between the anode and the cathode-side reference electrode. The anode-side voltage losses (anode IR losses, and anode non-ohmic overvoltage) were divided using the well-known current interruption technique.[4]

Redox cycling test.—In this study, redox cycling tests were conducted following a cycle protocol shown in Fig. 1c. This protocol is based on shutdown simulation tests of practical SOFC systems, as previously performed by Hanasaki et al.[4] We investigated anode IR losses, non-ohmic overvoltage, and degradation during/after this cycling test, to evaluate the SOFC degradation associated with redox cycling.

In the shutdown cycle test, we focus on fuel supply interruption, which is the major cause of Ni oxidation at the anode side. In one redox cycle of this test, the cell is operated with normal fuel supply (3%-humidified hydrogen) at a current density of 0.2 A cm^{-2} for 1 h. The fuel supply is then interrupted and the cell is operated for 1.5 h. The cell temperature is kept constant at 800°C. The fuel supply is then restored and this process repeated up to 50 cycles. After 50 cycles, the redox stability of the anodes was investigated.

High fuel utilization test.—High fuel utilization tests were performed to simulate downstream operation in realistic SOFC systems. For higher efficiency SOFCs, operation under higher fuel utilization (Uf) is required. To simulate downstream conditions in systems operated at Uf = 95%, 95%-humidified hydrogen gas was used as a model fuel, and the anode voltage was measured at a constant current density of 0.2 A cm^{-2}.

Microstructure observation.—A field-emission scanning electron microscope, coupled with energy-dispersive X-ray analysis (FESEM-EDX, Hitachi High-Technologies, S−5200, EDAX genesis 4000/JSM-700IF JEOL, Japan) and a focused-ion beam system coupled with SEM (FIB-SEM, HeliosNanolab 600i, FEI, USA) were applied to investigate the anode microstructures. The 3D microstructures were reconstructed from the FIB-SEM images using the software "Amira ver. 5.6".

Electrical conductivity measurement of the anode.—Electrical conductivity of the porous anode backbone layer consisting of LST and GDC in a 50:50 ratio by volume was measured using the four point probe technique. The porous layer was measured on the dense ScSZ electrolyte support, and the conductivity of the porous layer was calculated by subtracting the conductivity of the dense ScSZ electrolyte. This measurement was made in different humidified hydrogen atmospheres.

Results and Discussion

In this study, we fabricated two types of alternative anodes; Ni-impregnated anodes and Ni-GDC co-impregnated anodes.

Ni-impregnated anodes.—*X-ray diffraction analyses.*—Figure 2 shows XRD patterns of the LST-GDC composite anode powder sintered at 1300°C with ScSZ electrolyte and GDC interlayer powder, the LST-GDC composite anode powder sintered at 1300°C, and the pre-sintered LST-GDC anode powder after Ni-impregnation and thermal treatment at 1000°C. No secondary phases (such as $Ce_xZr_{1-x}O_2$) were detected. Although GDC buffer layers are generally sintered in the temperature range of 1100–1350°C,[28] it is possible that this material may react with zirconia to form a $Ce_xZr_{1-x}O_2$ solid solution, which would exhibit higher ohmic resistance. However, the cell performance was not affected by the introduction of the GDC interlayer, which was used here to prevent interfacial reaction between the LST and ScSZ. The LST-GDC anode powders calcined at 1300°C kept their original phase peaks, indicating that there is no obvious reaction between LST and GDC, as confirmed by Sun et al.[12] Moreover, the Ni-impregnated
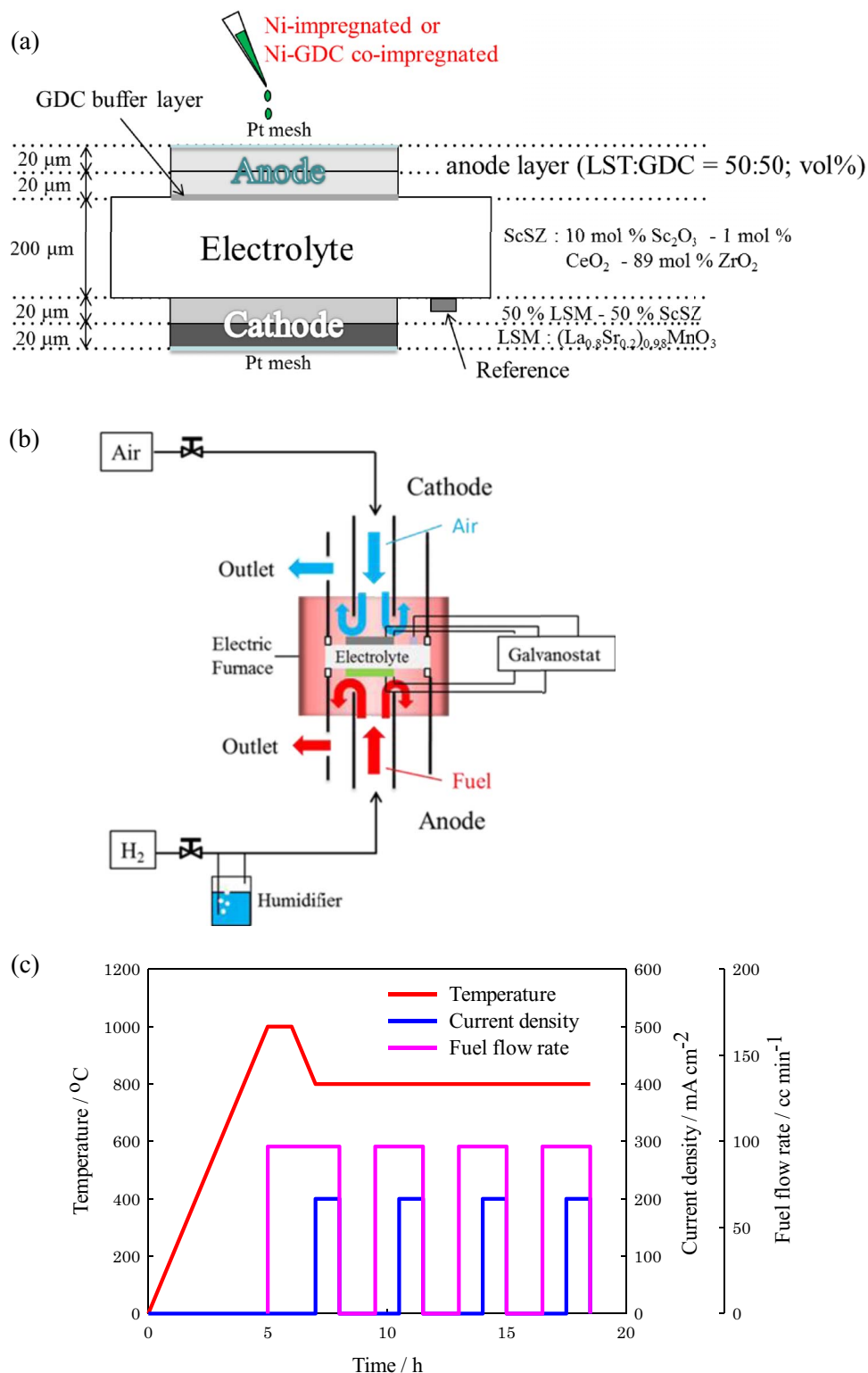
Figure 1. Schematic drawings of (a) the LST-GDC backbone single cell, (b) the experimental setup for the electrochemical measurements, and (c) the redox cycle protocol.[4]

LST-GDC anode powders show no secondary phase peaks indicating negligible reaction between Ni and LST or GDC. Therefore, thermal treatment at 1000°C for 2 h did not induce obvious reaction between the two phases. It is also possible that Ni could dissolve into the perovskite lattice,[29] but LST remained stable against possible cation doping at high temperature.

Microstructure.—The FIB-SEM micrograph in Fig. 3a shows the microstructure of the anode: the black areas correspond to pores; the dark gray areas to LST; the light gray areas to GDC; and the bright white spots to Ni nanoparticles. The Ni loading of this anode was 0.167 mg cm^{-2}. Figure 3a indicates that the microstructure forming the redox-stable backbone is essentially established during
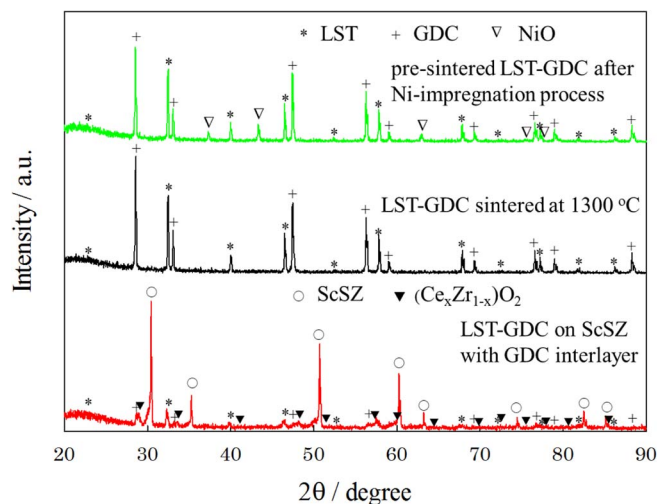
Figure 2. X-ray diffraction patterns for LST-GDC on ScSZ electrolyte sintered at 1300°C with GDC interlayer, LST-GDC sintered at 1300°C, and pre-sintered LST-GDC after Ni-impregnation and thermal treatment at 1000°C.

sintering, whilst nanostructure (i.e. Ni nanoparticles) results from the impregnation step. The 3D reconstructed microstructure of the Ni-impregnated anode after the initial reduction treatment is shown in Fig. 3; (b) all these materials, (c) LST backbones, (d) GDC backbones, and (e) Ni catalyst, respectively. Figures 3c, 3d and 3e clearly show sufficient connectivity between the electronic conductor LST, the MIEC GDC, and the Ni catalyst nanoparticles, respectively. From
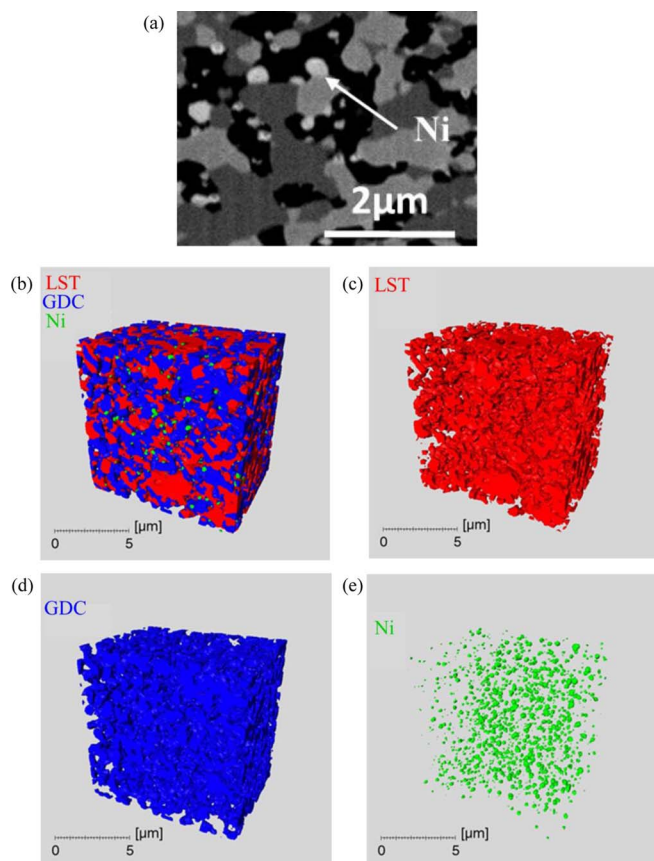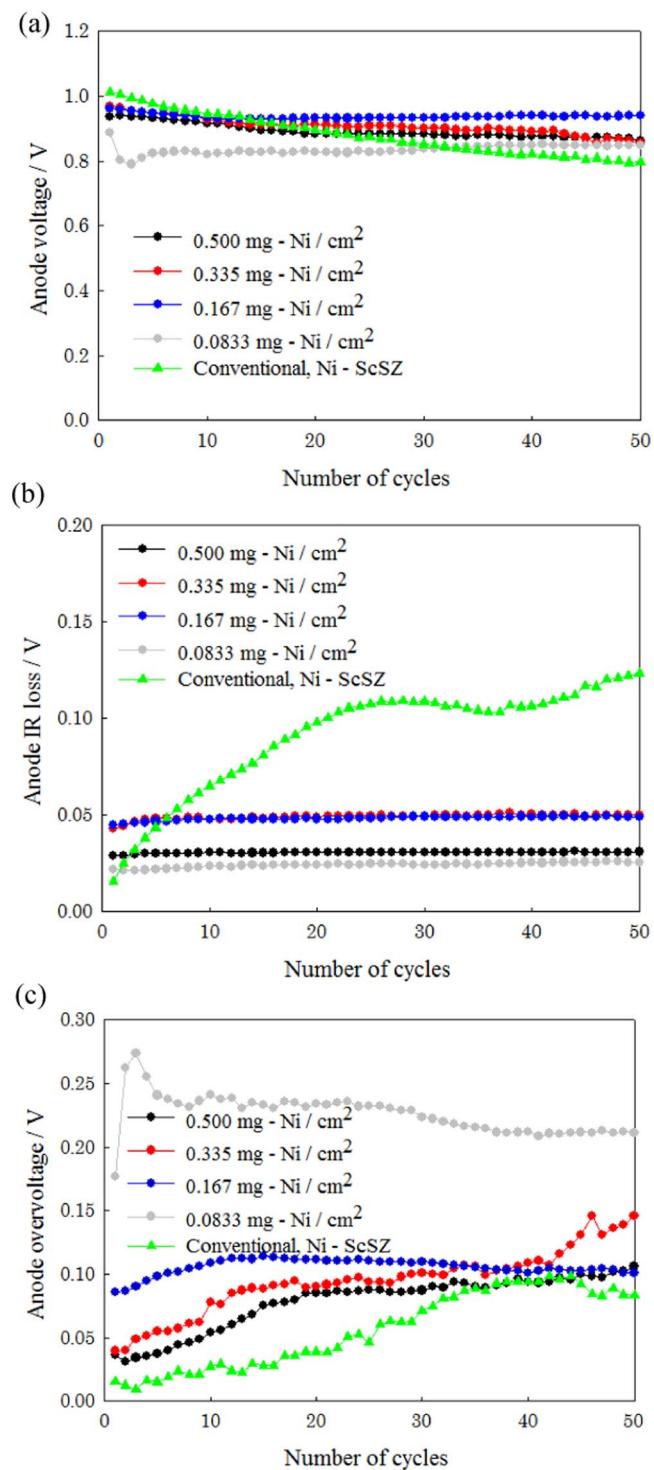

Figure 3. (a) FIB-SEM micrograph and 3D reconstructed FIB-SEM micrographs of a Ni-impregnated anode, (b) all materials, (c) LST, (d) GDC, and (e) Ni catalyst.

these micrographs, it is clear that the LST-GDC conducting oxides provide an electronic and ionic transport pathway, whilst Ni particles act as well-dispersed electrocatalysts, since a Ni content greater than 35 vol% would be needed to form a connected pathway for electron transport.[30] Attempts were also made to increase the Ni loading by performing multiple impregnation steps, but this caused aggregation of the Ni particles, and thus only one impregnation step was deemed necessary.

Redox stability.—The redox stability of Ni-impregnated anodes was investigated using a 50 cycle redox test. Figure 4 shows the change in anode voltage of Ni-impregnated anodes during the test, compared with that of a conventional Ni-ScSZ cermet anode.[4] From the change in anode voltage (Fig. 4a), it is clear that Ni-impregnated anodes exhibited better stability compared to the conventional anode. By separating the different overvoltages, Figs. 4b and 4c show that the anode IR losses and non-ohmic overvoltage of conventional anodes gradually increased, the reason for which has been previously determined by Hanasaki et al.[4] In addition, the anode IR losses for the Ni-impregnated anodes, remained stable even after redox cycling. Whilst the conducting path of conventional anodes can be destroyed due to Ni oxidation, the network structure of the MIEC oxide in Ni-impregnated anodes remains intact for electron transport, as confirmed by Shen et al.[23,24] In addition, agglomeration of the Ni catalyst nanoparticles on the anode backbone was prevented by optimizing the Ni loadings, to avoid increases in non-ohmic overvoltage. In this study, the optimal Ni loading to minimize performance degradation was 0.167 mg cm^{-2}. Figure 5 shows FIB-SEM micrographs of the Ni-impregnated anodes (a) before, and (b) after redox cycling. No obvious difference is observed in the LST-GDC anode backbone structure or Ni nanoparticle distribution, confirming that the microstructure is stable against Ni agglomeration. Chemical expansion of GDC due to the variation in P_{O_2} was previously reported by Bishop et al.,[31] however, the LST-GDC anode in this study has a porous structure increasing the stability against structural change by redox cycling, as shown in Fig. 5. Therefore, it is confirmed that using an alternative electron-conducting phase in the anode, rather than relying on Ni, can improve the cycling durability by avoiding Ni-oxidation-induced degradation.

Electrochemical characteristics of the Ni-impregnated anodes.— A schematic diagram explaining the difference in redox stability between Ni-impregnated anodes and conventional Ni-cermet anodes is shown in Fig. 6. In conventional cermet anodes, the interconnected electron-conducting Ni network expands upon oxidation (from Ni to NiO), and then Ni agglomeration can occur upon reduction back to Ni. This redox cycling breaks up the Ni-based backbone, reducing its electrochemical performance. On the other hand, Ni-impregnated MIEC oxide anodes are extremely stable against redox cycling and minimal microstructural change occurs. Moreover, the Ni catalyst loading can be optimized to suppress agglomeration. Figures 7 and 8 show the I-V characteristics of conventional and the Ni-impregnated anodes, with 3%-humidified H$_2$ and 80%-humidified H$_2$ fuels, respectively. The I-V characteristics of the Ni-impregnated anodes are still slightly lower (~0.97 V at 0.2 A cm^{-2} with 3%-humidified hydrogen fuel) compared to the conventional anode (~1.0 V at 0.2 A cm^{-2}). This may be caused by lower electronic conductivity of LST compared to that of Ni.
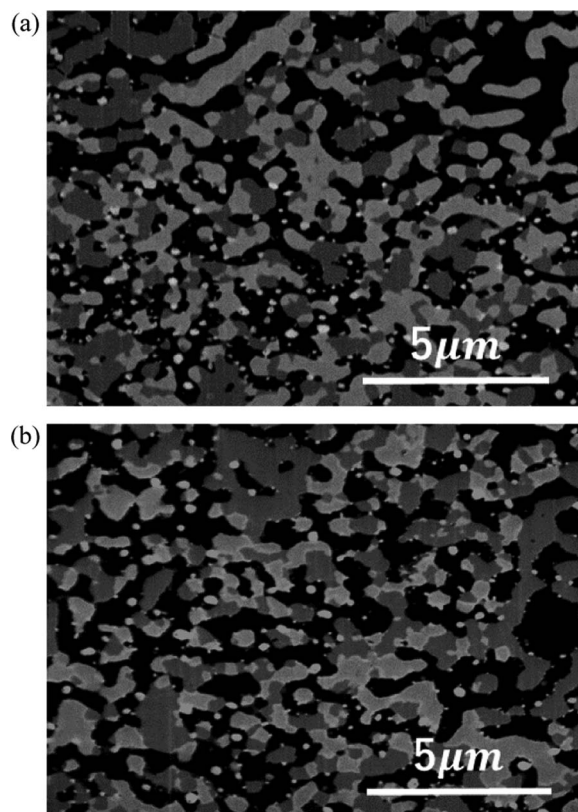
Ni-GDC co-impregnated anodes.—*GDC co-impregnation.*—In an attempt to further improve the electrochemical characteristics, GDC particles were co-loaded with Ni onto the anodes, via co-impregnation. The Ni-impregnated anodes have well-dispersed Ni catalyst nanoparticles in order to increase the density of electrode reaction sites, the double-phase boundaries (between the MIEC GDC and the gas phase), and the triple-phase boundaries (between the MIEC GDC, the electronic conducting LST, and the gas phase). In addition, co-impregnation of Ni and GDC can result in a Ni-GDC cermet supported on the stable LST-GDC anode backbone, to improve anode performance by preventing Ni catalyst agglomeration.

Figure 5. FIB-SEM micrographs of the Ni-impregnated anode (0.167 mg-Ni/cm^2) (a) before, and (b) after redox cycling. There is no clear change in the microstructure in terms of LST-GDC backbone and Ni distribution. The amount of Ni loading was optimized to become more stable against redox cycling.
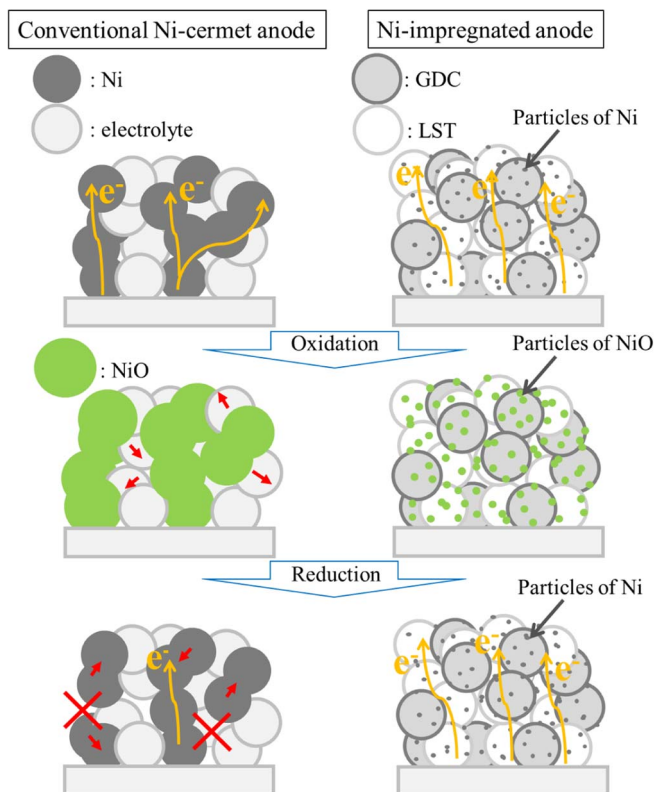

Figure 4. (a) Anode voltage, (b) anode IR losses, and (c) anode non-ohmic overvoltage of Ni-impregnated anodes and conventional Ni-cermet anodes over a 50-cycle durability test (3%-humidified hydrogen).

Figure 6. A schematic diagram on the difference between Ni-impregnated anodes and conventional Ni-cermet anodes against redox cycling.

According to several reports, impregnation of GDC has resulted in high performance and improved stability.[21–24]
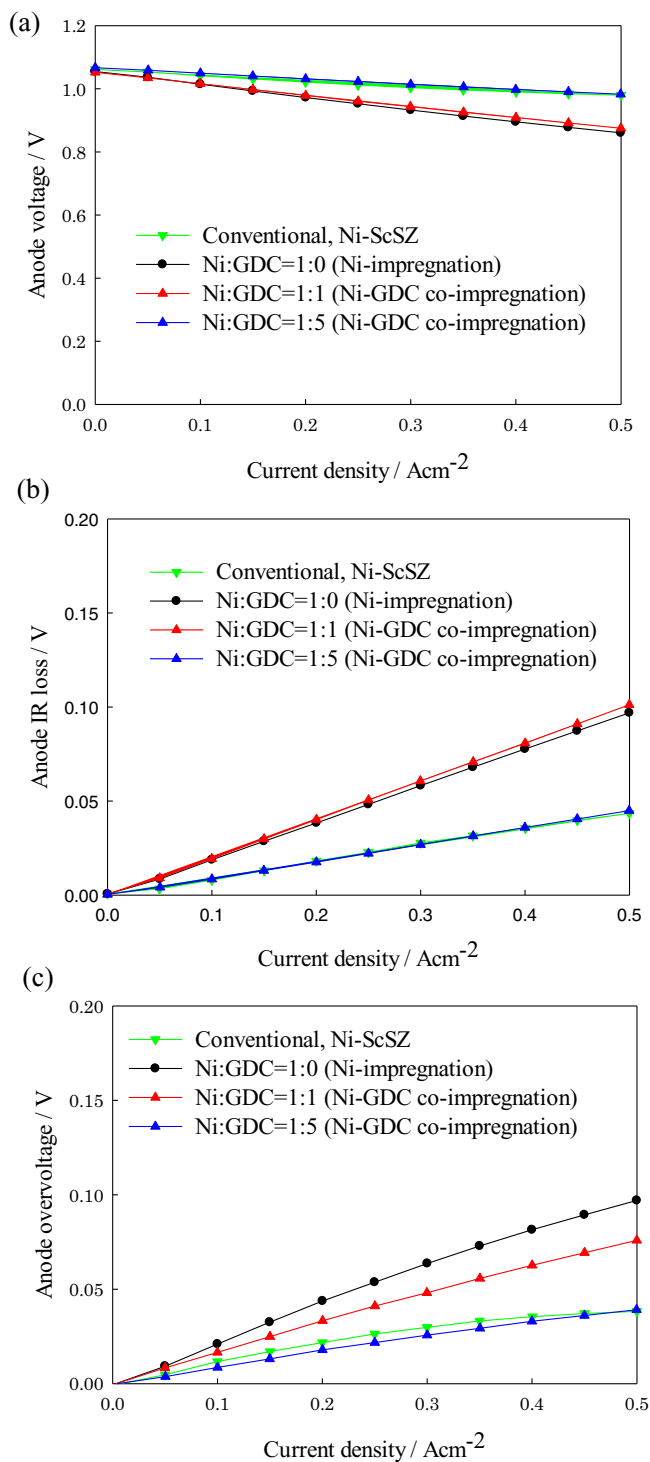
Effect on I-V characteristics.—Here, the effect of the co-impregnation on the I-V characteristics is described. Figures 7 and 8 show the I-V characteristics of a conventional Ni-ScSZ anode single cell, compared with three cells using the LST-GDC anode impregnated with Ni, or co-impregnated with different Ni:GDC ratios (i.e.

Figure 7. The I-V performances of conventional Ni-cermet anodes, Ni-impregnated anodes, and Ni-GDC co-impregnated anodes with 3%-humidified H_2 fuel, (a) anode voltage, (b) anode IR losses, and (c) anode overvoltage.

**Figure 8.** The I-V performances of conventional Ni-cermet anodes, Ni-impregnated anodes, and Ni-GDC co-impregnated anodes with 80%-humidified H_2 fuel, (a) anode voltage, (b) anode IR losses, and (c) anode overvoltage.

1:1 or 1:5 by volume). 3%-, or 80%-humidified H_2 fuel is utilized in Figs. 7 and 8, respectively. The Ni loading of all the impregnated anodes was fixed at 0.167 mg cm^{-2}. Co-impregnation with a Ni:GDC ratio of 1:1, does not result in any obvious difference in anode IR losses (see Figs. 7b and 8b), but it is clear that co-impregnation results in reduced anode non-ohmic overvoltage (see Figs. 7c and 8c). This may be due to the increased number of available reaction sites by additionally impregnating GDC particles.

In addition, the anode IR loss and the anode non-ohmic overvoltage (see Figs. 7b, 7c, 8b, and 8c) both decrease as the ratio of GDC in the anode increases, despite all the co-impregnated anodes having the same pre-sintered LST-GDC conducting backbones. This result suggests that GDC co-loaded particles contribute to both an increase in the number of reaction sites, and the formation of additional continuous conducting pathways. The co-impregnated anode with a Ni:GDC
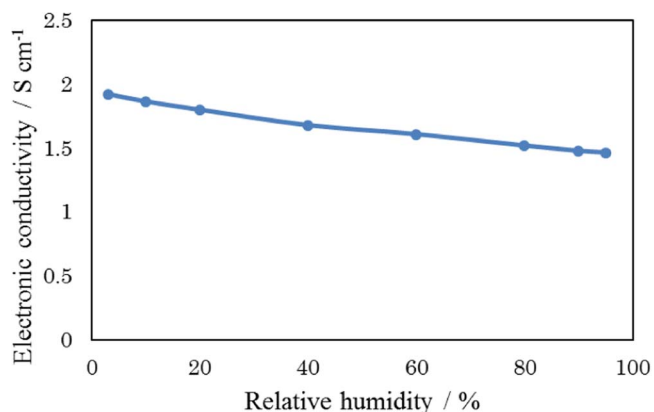
Figure 9. Electronic conductivity of the LST-GDC (50:50 ratio in volume) conducting porous backbone.

ratio of 1:5 exhibited comparable I-V characteristics ($\sim$1.0 V at 0.2 A cm^{-2} with 3%-humidified hydrogen fuel) to the conventional Ni-ScSZ cermet anode for 3%-humidified hydrogen fuel, whilst lower I-V performance was obtained for the heavily humidified hydrogen fuel, due in part to decreased electronic conductivity in the LST-GDC porous oxide backbone at higher humidity, as shown in Fig. 9. The electrical conductivity of LST decreases with increasing oxygen partial pressure, confirming previous results obtained by Marina et al.[11]
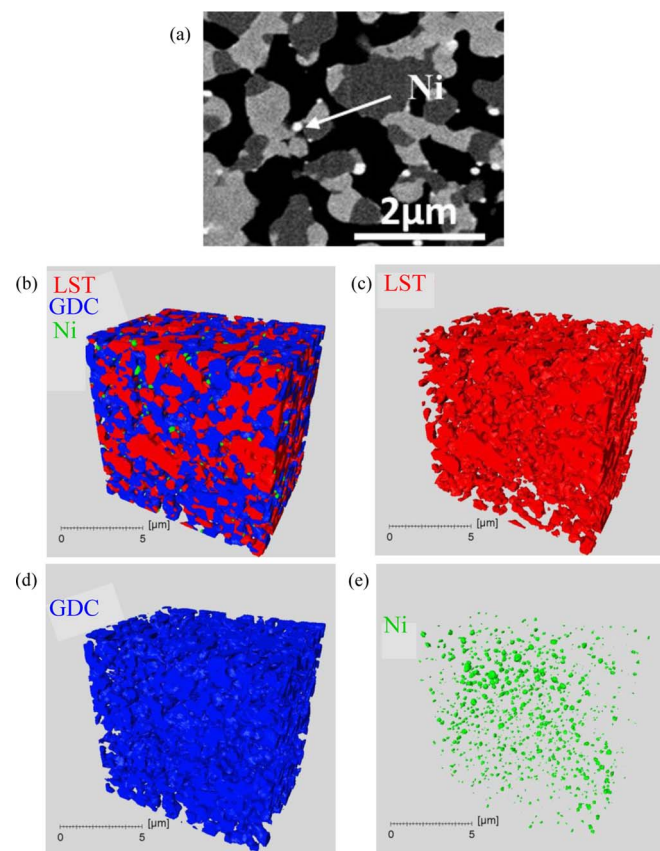
Figure 10. (a) FIB-SEM micrograph and 3D reconstructed FIB-SEM micrographs of a Ni-GDC co-impregnated anode, (b) all materials, (c) LST, (d) GDC, and (e) Ni catalyst. The Ni catalyst particles observed in Fig. 10e are more highly dispersed, than those observed in Fig. 3e.
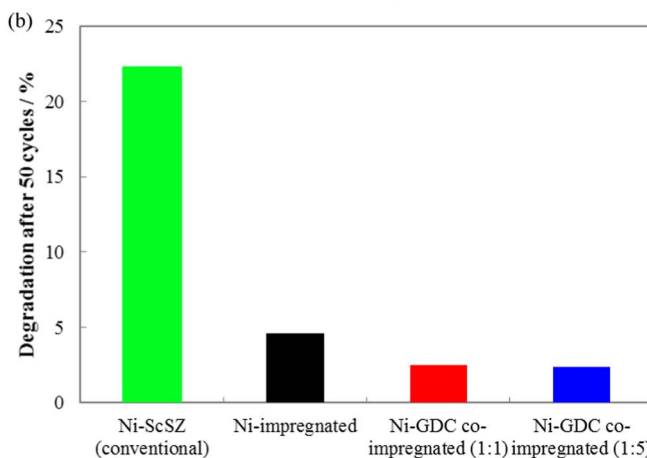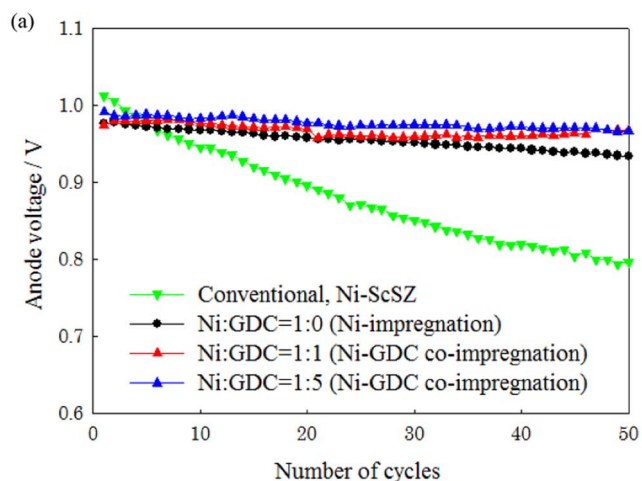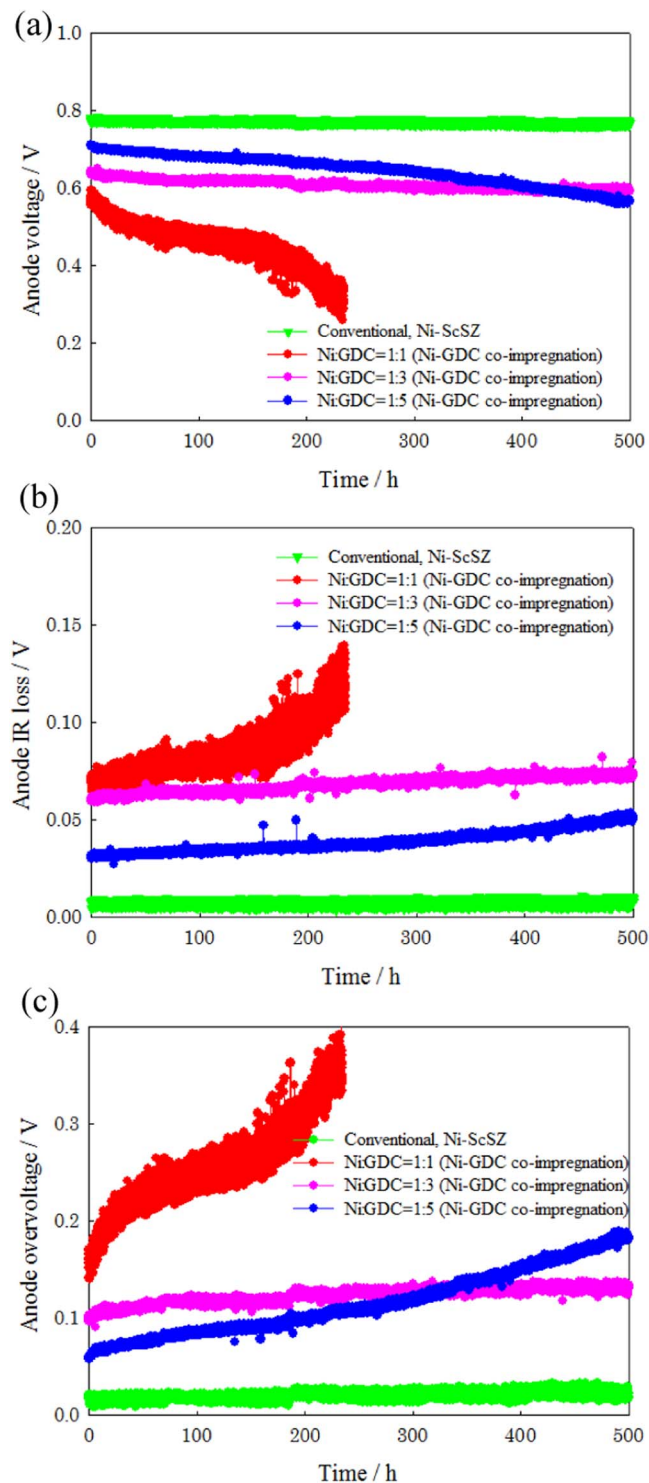

Figure 11. (a) Anode voltage and (b) degradation of Ni-impregnated anodes, Ni-GDC co-impregnated anodes and conventional Ni-cermet anodes after the 50-cycling durability tests.

Microstructure.—The FIB-SEM micrograph in Fig. 10a shows the microstructure of the Ni-GDC co-impregnated anode with a Ni:GDC ratio of 1:1. The black areas correspond to pores; the dark gray areas to LST; the light gray areas to GDC; and the bright white spots to Ni nanoparticles. The 3D reconstructed microstructure after the initial reduction treatment is shown in Fig. 10b–10e; (b) all materials, (c) LST backbones, (d) GDC backbones, and (e) Ni catalyst. Figure 10a also indicates that a high density of Ni catalysts nanoparticles are loaded on the LST-GDC conducting backbone. In addition, by comparing Fig. 10e with Fig. 3e, the Ni catalyst nanoparticles in the co-impregnated anode seem to be more highly dispersed, with a smaller grain size. By evaluating the difference in Ni particle size distribution between the Ni-impregnated anode and the Ni-GDC co-impregnated anode, it is evident that GDC co-impregnation results in smaller Ni nanoparticle size. This is attributed to suppressed Ni sintering due to co-impregnation with GDC, leading to a decrease in anodic non-ohmic overvoltage.

Redox stability.—Figure 11 shows the change in anode voltage of the Ni-GDC co-impregnated anodes compared with those of Ni-impregnated anodes, and conventional anodes. The co-impregnated anodes had better redox stability than the conventional anode, and were also more stable than the Ni-impregnated anodes. This suggests that GDC co-impregnation suppresses Ni agglomeration to achieve better redox stability.
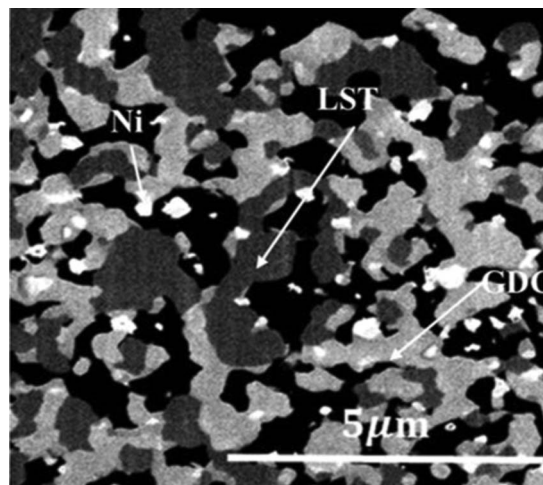
Durability at high fuel utilization.—In order to simulate the downstream region of practical SOFC systems, long-term durability tests

(a)

(b)

(c)

Figure 12. (a) Anode voltage, (b) anode IR losses, and (c) anode overvoltage of the Ni-GDC co-impregnated anodes and the conventional Ni-cermet anode during high fuel utilization tests with constant current density, 0.2 A cm^{-2}.

Figure 13. FIB-SEM micrograph of the Ni-GDC co-impregnated anode with a Ni:GDC of 1:3 after the high fuel utilization test. This figure indicates grain growth of Ni particles, by comparing the sample before the durability test showing Fig. 10a.

in the porosity may also be partly responsible for this degradation. The co-loaded GDC particles may contribute to the formation of an improved conducting pathway, and an increase in the number of electrode reaction sites, but too much GDC co-loaded onto the anode may suppress fuel diffusion at high fuel utilization.

Figure 13 shows a FIB-SEM micrograph of a co-impregnated Ni-GDC anode with a Ni:GDC ratio of 1:3 after the high fuel utilization durability test. This anode exhibited the best tolerance against high oxygen partial pressure among all the co-impregnated anodes. Compared with the initial microstructure (see Fig. 10a), the Ni catalyst nanoparticles increase in size, although the MIEC backbone microstructure appears to remain unchanged. The Ni catalyst nanoparticles in the co-impregnated anodes can be easily oxidized, as the anode voltage at the co-existing boundary between Ni and NiO is 0.701 V at 800°C.[2] In this case, the Ni nanoparticles were oxidized, losing their catalytic activity, because the initial anode voltage of the co-impregnated anodes was lower (< 0.701 V) for the heavily-humidified hydrogen fuel (95%-humidified H$_2$), leading to the fastest degradation in co-impregnated anodes with a Ni:GDC ratio of 1:1. It is therefore necessary to further improve the initial performance and/or to apply more stable alternative electrocatalyst materials in the downstream of the SOFC systems for application at higher fuel utilization.

Conclusions

An oxide-based SOFC anode backbone was fabricated using electron conducting LST and mixed ionic-electronic conducting GDC. These materials were chosen for their improved stability against redox cycling compared to conventional Ni-ScSZ. Ni catalyst nanoparticles were decorated onto these backbones via impregnation. Co-impregnation of GDC with Ni further suppresses anode IR losses and non-ohmic overvoltage to achieve better durability and performance. Ni-GDC co-impregnated anodes exhibit comparable I-V performance to conventional Ni-cermet anodes. As the GDC co-loading ratio increases, this results in improved I-V characteristics and better redox stability, due to more finely dispersed co-loaded GDC particles. On the other hand, at much higher co-loading ratios (i.e. Ni:GDC = 1:5) the performance deteriorates faster in the presence of high humidity fuel, due to the suppression of mass diffusion of the fuel supply within the porous anode. Consequently, the optimal co-loading ratio of Ni:GDC was found to be 1:3 in this study. Whilst the electrochemical properties at very high fuel utilization must be further improved, Ni-GDC co-impregnated anodes with redox stable backbone structure

were conducted at high fuel utilization (i.e. under higher oxygen partial pressure). Changes in anode voltage of the Ni-GDC co-impregnated anodes and the conventional Ni-ScSZ anode are shown in Fig. 12. The conventional cermet anode was more stable in this test despite its poor redox stability, while all the co-impregnated anodes deteriorated. The degradation of the co-impregnated anode with a Ni:GDC ratio of 1:5 was more obvious compared to that of the anode using a Ni:GDC ratio of 1:3. An increase in concentration overvoltage causing a decrease

could be a promising alternative robust anode for high fuel utilization operation of SOFC systems.

References

1. K. Sasaki, H-W. Li, A. Hayashi, J. Yamabe, T. Ogura, and S. M. Lyth, editors. *Hydrogen Energy Engineering: a Japanese perspective*, Japan: Springer; ISBN 978-4-431-56040-1 (2016).
2. T. Kawasaki, J. Sugimoto, Y. Tachikawa, Y. Shiratori, S. Taniguchi, and K. Sasaki, *ECS Trans*, **8**(1), 1345 (2015).
3. Q. Fang, L. Blum, R. Peters, M. Peksen, P. Batfalsky, and D. Stolten, *Int. J. Hydro. Energy*, **40**(2), 1128 (2015).
4. M. Hanasaki, C. Uryu, T. Daio, T. Kawabata, Y. Tachikawa, S. M. Lyth, Y. Shiratori, S. Taniguchi, and K. Sasaki, *J. Electrochem. Soc.*, **161**(9), F850 (2014).
5. Y. Guan, Y. Gong, W. Li, J. Gelb, L. Zhang, G. Liu, X. Zhang, X. Song, C. Xia, Y. Xiong, H. Wang, Z. Wu, and Y. Tian, *J. Power Sources*, **196**(24), 10601 (2011).
6. M. H. Pihlatie, A. Kaiser, M. Mogensen, and M. Chen, *Solid State Ionics*, **189**(1), 82 (2011).
7. L. Holzer, B. Iwanschitz, Th. Hocker, L. Keller, O. Pecgo, G. Sartoris, Ph. Gasser, and B. Muench, *J. Power Sources*, **242**, 179 (2013).
8. L. Holzer, B. Iwanschitz, Th. Hocker, B. Munch, M. Preatat, D. Wiedenmann, U. Vogt, P. Holtappels, J. Sfeir, A. Mai, and Th. Graule, *J. Power Sources*, **196**(3), 1279 (2011).
9. Z. Wang and M. Mori, *J. Fuel Cell Sci. Technol.*, **8**(5), 051018 (2011).
10. Z. Wang, M. Mori, and T. Itoh, *J. Electrochem. Soc.*, **157**(12), B1783 (2010).
11. O. A. Marina, N. L. Canfield, and J. W. Stevenson, *Solid State Ionics*, **149**(1–2), 21 (2002).
12. X. Sun, S. Wang, Z. Wang, X. Ye, T. Wen, and F. Huang, *J. Power Sources*, **183**(1), 114 (2008).
13. K. B. Yoo and G. M. Choi, *Solid State Ionics*, **192**(1), 515 (2011).
14. K. B. Yoo and G. M. Choi, *Solid State Ionics*, **180**(11–13), 867 (2009).
15. G. Chen, H. Kishimoto, K. Yamaji, K. Kuramoto, and T. Horita, *J. Electrochem. Soc.*, **162**(3), F223 (2015).
16. M. R. Pillai, I. Kim, D. M. Bierschenk, and S. A. Barnett, *J. Power Sources*, **185**(2), 1086 (2008).
17. T. Z. Sholklapper, C. P. Jacobson, S. J. Visco, and L. C. De Jonghe, *Fuel Cells 08*, **8**(5), 303 (2008).
18. S. P. Jiang, *Mater. Sci. Eng.*, **418**(1–2), 199 (2006).
19. J. Irvine, D. Neagu, M. Verbraeken, C. Chatzichistodoulou, C. Graves, and M. Mogensen, *Nature Energy*, **1**(1), 15014 (2016).
20. K. Park, S. Lee, G. Bae, and J. Bae, *Renewable Energy*, **83**, 483 (2015).
21. X. J. Chen, Q. L. Liu, S. H. Chan, N. P. Brandon, and K. A. Khor, *Fuel Cells Bulletin*, **2007**(6), 12 (2007).
22. W. Wang, S. P. Jiang, A. Y. Tok, and L. Luo, *J. Power Sources*, **159**(1), 68 (2006).
23. X. Shen and K. Sasaki, *J. Power Sources*, **320**, 180 (2016).
24. X. Shen and K. Sasaki, *ECS Trans*, **68**(1), 1447 (2015).
25. A. M. Hussain, J. V. T. Høgh, T. Jacobsen, and N. Bonanos, *Int. J. Hydro. Energy*, **37**(5), 4309 (2012).
26. A. M. Hussain, J. V. T. Høgh, W. Zhang, and N. Bonanos, *J. Power Sources*, **216**, 308 (2012).
27. V. Yurkiv, G. Constantin, A. Gondolini, E. Mercadelli, A. Sanson, L. Dessemond, and R. Costa, *ECS Trans*, **68**(1), 1517 (2015).
28. M. Yang, A. Yan, M. Zhang, Z. Hou, Y. Dong, and M. Cheng, *J. Power Sources*, **175**(1), 345 (2008).
29. Y. Sun, J. Li, Y. Zeng, B. S. Amirkhiz, M. Wang, Y. Behnamian, and J. Luo, *J. Mater. Chem. A*, **3**, 11048 (2015).
30. A. McEvoy, Anodes, in: S.C. Singhal and K. Kendall, editors. *High temperature solid oxide fuel cells: fundamentals, design, and applications*, Elsevier, Oxford, pp. 168 (2003).
31. S. R. Bishop, K. L. Duncan, and E. D. Wachsman, *ECS Trans*, **1**(7), 13 (2006).